

Sliding mode adaptive neural network control for hybrid visual servoing of underwater vehicles



Jian Gao^{a,*}, Xuman An^a, Alison Proctor^b, Colin Bradley^c

^a School of Marine Science and Technology, Northwestern Polytechnical University, Xi'an 710072, China

^b Ocean Floor Geophysics Inc., Burnaby, BC, Canada V5J 5J3

^c Department of Mechanical Engineering, University of Victoria, Victoria, BC, Canada V8P 5C2

ARTICLE INFO

Keywords:

Underwater vehicles
Hybrid visual servoing
Neural networks
Adaptive sliding mode control
Dynamic uncertainties

ABSTRACT

In this paper, a hybrid visual servo (HVS) controller is proposed for underwater vehicles, in which a combination of the vehicle's 3-D Cartesian pose and the 2-D image coordinates of a single feature is exploited. A dynamic inversion-based sliding mode adaptive neural network control (DI-SMANNNC) method is developed for tracking the HVS reference trajectory generated from a constant target pose. A single hidden-layer (SHL) feedforward neural network, in conjunction with an adaptive sliding mode controller, is utilized to compensate for dynamic uncertainties. The adaptation laws of neural network weight matrices and control gains are designed to ensure the asymptotical stability of tracking errors and the ultimate uniform boundedness (UUB) of neural network weight matrices. The main advantage of the proposed DI-SMANNNC over conventional sliding model neural network controllers lies in the fact that the knowledge of the bounds on system uncertainties and neural approximation errors is not required to be previously known. Simulation results are presented to validate the effectiveness of the developed controller, especially the robustness with respect to dynamic modeling uncertainties and camera calibration errors.

1. Introduction

Visual servoing, also known as vision-based control, uses a camera system to provide feedback signals for a robotic system, such that a set of visual features moves through the image frame to reach a desired configuration (Chaumette and Hutchinson, 2006, 2007). Visual servoing methods fall into three categories based on the type of information used in the feedback signals: (1) Position-based visual servoing (PBVS), where feedback is defined in terms of the relative 3-D Cartesian information reconstructed from obtained images, (2) Image-based visual servoing (IBVS), where feedback is directly defined in terms of image feature coordinates, and (3) Hybrid visual servoing (HVS), also called 2.5-D visual servoing, where a combination of partially reconstructed 3-D Cartesian information and 2-D image-space information is used in the feedback control design.

Over the past few decades, visual servoing has gained a lot of research interests with applications in industrial, aerial, and wheeled robots. This technology is applied to dynamic positioning (DP) or station keeping of underwater vehicles operated near the seafloor or subsea facilities since the 2000s (Sørensen, 2011). For an underwater vehicle, visual servoing uses low-cost visual features rather than

acoustic beacons, and inherently has the advantage of higher resolution and update-rate compared to acoustic positioning systems. Lots et al. (2000) applied an HVS technique to maintain the position of an underwater vehicle with respect to a fixed planar target. The dynamic controller was simplified by using a steady thrust mapping with saturation. In another paper, Lots et al. (2001) introduced an IBVS technique with a proportional-integral-derivative (PID) controller to solve a similar station-keeping problem, where only the surge and sway degrees-of-freedom (DOF) were considered. Silpa-Anan et al. (2001) designed and implemented a positioning controller for an underwater vehicle using a standard computed torque method, based on the position and velocity feedback provided by a binocular camera system. Caccia et al. (2007) estimated the motion of near-seafloor vehicles using a laser-triangulation sensor with optical correction, and designed and implemented high-precision motion control using a gain-scheduling PI controller. Bechlioulis et al. (2013) described a PBVS system to stabilize an underwater vehicle, where the state vector was estimated using an extended Kalman filter (EKF). Heshmati-alamdari et al. (2014) employed self-triggered model predictive control (MPC) in a PBVS approach based on a kinematic model for an underactuated underwater vehicle, in which the vehicle pose was estimated using a

* Corresponding author.

E-mail address: jiangao@nwpu.edu.cn (J. Gao).

visual system. Hua et al. (2014) proposed a homography-based visual servoing approach to stabilize a fully-actuated vehicle by exploiting the homography matrix containing the transformation information between the current and desired camera coordinates. Li et al. (2015) proposed a visual docking method for an underwater vehicle using two cameras at the nose. A two-layer control system composed a homing controller and an attitude tracking controller was designed. The authors (Gao et al., 2016a) proposed a hierarchical IBVS control architecture for underwater vehicles, composed of a nonlinear model predictive kinematic controller and an adaptive neural network dynamic controller. In a recent work (Gao et al., 2016b), we designed a PBVS controller for underwater vehicles to track a time-varying reference trajectory based on the estimated pose by an unscented Kalman filter with visual measurements.

In summary, the PBVS approach, which is mostly employed for underwater vehicles, simplifies the controller design, but relies heavily on exact camera calibration to reconstruct the vehicle's 3-D pose by fusing visual and motion information. The aforementioned IBVS and HVS controllers use only visual information from multiple features for feedback control and orientation reconstruction, as those applied to robot manipulators. In a real underwater environment, light is highly attenuated by the water mass and scattered by suspended particles; which make it hard to identify and locate multiple features with low-quality images. The orientation reconstructed from images by a conventional HVS approach is sensitive to image noises and camera calibration errors. Another drawback of IBVS and classical HVS algorithms lies in that only local asymptotic stability can be obtained (Chaumette and Hutchinson, 2006, 2007), because the dimension of visual feedback is greater than the number of system DOFs.

In practice, different to a robotic manipulator that uses only cameras for motion detection, a work-class underwater vehicle is also equipped with various motion sensors, including a depth sensor, an altimeter, an attitude and heading reference system, and a Doppler velocity log to provide position, orientation, and velocity information for feedback control. In this paper, motivated by this fact, we propose a novel HVS approach by integrating the visual information of a single point-like feature and the global pose information into the system state (Gao et al., 2016c).

An underwater vehicle is a highly nonlinear, heavily coupled system with uncertain hydrodynamic parameters and suffering from environmental disturbances, which makes the control task challenging (Shi et al., 2017). Various nonlinear control methods have been developed, including sliding mode control (SMC) (Zhu and Sun, 2013; Zhang and Chu, 2012; Cui et al., 2016), robust adaptive control (Fischer et al., 2014; Zool et al., 2016; Soylu et al., 2016), neural network (NN) control (Zhang et al., 2009; Du et al., 2013; Chu et al., 2016; Peng and Wang, 2017), model predictive control (Shen et al., 2016b; Shen et al., 2017), energy-based control (Valentinis et al., 2015), and active disturbance rejection control (Shen et al., 2016a). In particular, neural network-based model reference adaptive control (MRAC) (Johnson and Kannan, 2005) has showed an excellent performance even in the presence of uncertainties through comprehensive simulations and in-water tests (Proctor, 2014). In NN-based adaptive controllers, linearly parameterized radial basis function (RBF) and nonlinearly parameterized single hidden-layer (SHL) neural networks are widely employed as adaptive elements to model continuous nonlinear dynamics as well as all uncertainties in the plant. An RBF NN acts as a universal approximator only for suitably chosen basis functions, and the number of required basis functions increases dramatically with the dimension of input vectors. By conducting a detailed comparison of these two NNs in the flight control of unmanned aerial vehicles, Anderson et al. (2009) indicated that an RBF NN controller has a slower update rate than an SHL one, and is more susceptible to overfitting errors and improper learning.

Conventionally, the closed-loop stability of an NN-based control system is restricted to ultimate uniform boundedness (UUB) because

of residual NN approximation errors (Johnson and Kannan, 2005; Lewis, 1999). A direct method for removing the inherent error is to integrate a robustifying term, such as SMC, into the NN-based adaptive control law (Wai and Muthusamy, 2013). Patre et al. (2008) incorporated a robust integral of the sign of the error (RISE) feedback term with an NN-based feedforward compensator to achieve semi-global asymptotic tracking for uncertain dynamic systems. However, the asymptotical stability of control systems still relies on the assumption that the upper bounds of ideal network weights and approximation errors are previously known, especially for nonlinear SHL NNs.

To remove this assumption, Sun et al. (2011) designed an RBF NN-based sliding mode adaptive controller for trajectory tracking of robot manipulators. The enhanced asymptotical convergence of tracking errors was achieved by incorporating an SMC-like time-varying robustifying term with adaptive gains driven by error signals. Unfortunately, this approach cannot be directly applied to nonlinear SHL NN-based adaptive controllers.

In this paper, motivated by the adaptive SMC designed by Li and Xu (2010), we present a dynamic inversion-based sliding mode adaptive neural network controller (DI-SMANNC) for the HVS control of underwater vehicles to handle vehicle dynamic uncertainties, including external disturbances. Compared with the existing underwater visual servo systems, the main contributions of the proposed approach are two-folds.

- (1) This proposed HVS scheme is more robust and practical than conventional visual servoing approaches of underwater vehicles, because only a single visual feature is required, which reduces the system complexity and computational load of image processing. The orientation directly obtained by motion sensors are more reliable than those reconstructed from images in a classic HVS system.
- (2) The control gains in the proposed DI-SMANNC are updated online to ensure asymptotical stability without any knowledge of the upper bounds on uncertainties and neural network weights, which simplifies the controller design. This method is also valid for other nonlinear robotic systems, e.g., manipulators as presented in Wai and Muthusamy (2013) and Sun et al. (2011).

The remainder of this paper is organized as follows. Section 2 describes the mathematical formulation of the HVS problem, including the models for an underwater vehicle and a downward-looking visual system. Section 3 details the DI-SMANNC development for HVS of underwater vehicles. The asymptotical stability of visual servoing errors and the boundedness of neural network weight matrices are proven by a Lyapunov method. In Section 4, simulation studies with a six DOF underwater vehicle are presented to illustrate the performance of the proposed controller, and test the robustness with respect to dynamic modeling uncertainties and camera calibration errors. Finally, some concluding remarks are provided in Section 5.

Notations. Let \mathbb{R} denote the real number, \mathbb{R}^n the real n -vectors, and $\mathbb{R}^{m \times n}$ the real $m \times n$ matrices. $\mathbf{0}_{m \times n}$ is an $m \times n$ zero matrix consisting of all 0 s, and \mathbf{I}_n is an $n \times n$ identity matrix. Superscript “T” indicates matrix transposition. We use the notation $\|\mathbf{x}\| = \sqrt{\mathbf{x}^T \mathbf{x}}$ to indicate the 2-norm of vector \mathbf{x} for any $\mathbf{x} \in \mathbb{R}^n$. Given $\mathbf{A} = [a_{ij}]$, the Frobenius norm is defined by $\|\mathbf{A}\|_F^2 = \text{tr}(\mathbf{A}^T \mathbf{A}) = \sum a_{ij}^2$ with $\text{tr}(\cdot)$ being the trace operation.

2. Problem formulation

2.1. Modeling of underwater vehicles

This section describes the underwater vehicle model presented by Fossen (2002) for control design and simulations. The kinematic and dynamic equations of an underwater vehicle is developed with the

global earth-fixed frame, \mathcal{G} , and the body-fixed frame, \mathcal{B} . The kinematic equations of underwater vehicles are given by

$$\dot{\boldsymbol{\eta}} = \mathbf{J}_{\boldsymbol{\eta}}(\boldsymbol{\eta}_2) \mathbf{v} \quad (1)$$

where the generalized pose vector $\boldsymbol{\eta} = [x, y, z, \varphi, \theta, \psi]^T \in \mathbb{R}^6$ contains the global position $\boldsymbol{\eta}_1 = [x, y, z]^T$ represented in \mathcal{G} and the Euler angles $\boldsymbol{\eta}_2 = [\varphi, \theta, \psi]^T$, and the generalized velocity vector $\mathbf{v} = [u, v, w, p, q, r]^T \in \mathbb{R}^6$ is composed of the linear velocity vector, $\mathbf{v}_1 = [u, v, w]^T$, and the angular velocity vector, $\mathbf{v}_2 = [p, q, r]^T$, both represented in \mathcal{B} . $\mathbf{J}_{\boldsymbol{\eta}}: \mathbb{R}^3 \rightarrow \mathbb{R}^{6 \times 6}$ is the transformation matrix relating two frames, expressed as

$$\mathbf{J}_{\boldsymbol{\eta}}(\boldsymbol{\eta}_2) = \begin{bmatrix} \mathbf{R}_b^g(\boldsymbol{\eta}_2) & \mathbf{0}_{3 \times 3} \\ \mathbf{0}_{3 \times 3} & \mathbf{T}_{\theta}(\boldsymbol{\eta}_2) \end{bmatrix} \quad (2)$$

where $\mathbf{R}_b^g(\boldsymbol{\eta}_2)$ denotes the Euler angle rotation matrix, and $\mathbf{T}_{\theta}(\boldsymbol{\eta}_2)$ is the angular velocity transformation matrix, given as

$$\mathbf{R}_b^g(\boldsymbol{\eta}_2) = \begin{bmatrix} \cos \psi \cos \theta & -\sin \psi \cos \varphi + \cos \psi & \sin \psi \sin \varphi + \cos \psi \\ & \sin \theta \sin \varphi & \sin \theta \cos \varphi \\ \sin \psi \cos \theta & \cos \psi \cos \varphi + \sin \psi \sin \theta & -\cos \psi \sin \varphi + \sin \psi \\ & \sin \varphi & \sin \theta \cos \varphi \\ -\sin \theta & \cos \theta \sin \varphi & \cos \theta \cos \varphi \end{bmatrix} \quad (3)$$

$$\mathbf{T}_{\theta}(\boldsymbol{\eta}_2) = \begin{bmatrix} 1 & \sin \varphi \tan \theta & \cos \varphi \tan \theta \\ 0 & \cos \varphi & -\sin \varphi \\ 0 & \sin \varphi / \cos \theta & \cos \varphi / \cos \theta \end{bmatrix} \quad (4)$$

In practice, the depth z is affected by deviations of water level and barometric pressure, and is not suitable for absolute positioning control of an underwater vehicle during operations. In this paper, the height above the seafloor, h , is preferred to describe the vertical position instead of depth, which can be obtained by an altimeter, as shown in Fig. 1. The time derivative of h is calculated as

$$\dot{h} = -\dot{z} = -\mathbf{R}_3(\boldsymbol{\eta}_2) \mathbf{v}_1 \quad (5)$$

where $\mathbf{R}_3(\boldsymbol{\eta}_2) = [-\sin \theta \quad \cos \theta \sin \varphi \quad \cos \theta \cos \varphi]$ is the third row of $\mathbf{R}_b^g(\boldsymbol{\eta}_2)$ in (3).

The underwater vehicle dynamics are given as

$$\mathbf{M}_{RB} \dot{\mathbf{v}} + \mathbf{C}_{RB}(\mathbf{v}) \mathbf{v} + \mathbf{M}_{AM} \dot{\mathbf{v}}_r + \mathbf{C}_{AM}(\mathbf{v}_r) \mathbf{v}_r + \mathbf{D}(\mathbf{v}_r) \mathbf{v}_r + \mathbf{g}(\boldsymbol{\eta}_2) = \mathbf{B} \mathbf{T}(\boldsymbol{\delta}) + \boldsymbol{\tau}_d \quad (6)$$

where \mathbf{v}_r is the vehicle's velocity relative to the ambient water mass

given by

$$\mathbf{v}_r \triangleq \mathbf{v} - \begin{bmatrix} \mathbf{R}_s^b(\boldsymbol{\eta}_2) \mathbf{v}_c \\ \mathbf{0}_{3 \times 1} \end{bmatrix} \in \mathbb{R}^6 \quad (7)$$

with $\mathbf{v}_c \in \mathbb{R}^3$ being the constant global translational water velocity, and $\mathbf{R}_s^b(\boldsymbol{\eta}_2) = \mathbf{R}_b^g(\boldsymbol{\eta}_2)^T$. \mathbf{M}_{RB} and \mathbf{M}_{AM} are the positive definite inertial matrices of rigid-body and added mass, respectively. $\mathbf{C}_{RB}(\cdot)$ and $\mathbf{C}_{AM}(\cdot)$ are the corresponding Coriolis and centripetal matrices. The damping matrix $\mathbf{D}(\mathbf{v}_r) = \mathbf{D}_l + \mathbf{D}_q(\mathbf{v}_r)$ includes the linear and quadratic damping terms. $\mathbf{g}(\boldsymbol{\eta}_2)$ represents the restoring forces and moments produced by the gravity and buoyancy. $\mathbf{T}(\cdot)$ is the thrust force vector produced by l thrusters, and $\boldsymbol{\delta} \in \mathbb{R}^l$ is the control signals. It is assumed that the thruster response is fast enough, and there exists a nonlinear non-decreasing relationship between the thrust force and the control signal. $\mathbf{B} \in \mathbb{R}^{6 \times l}$ is the constant thruster mapping matrix. The underwater vehicle is considered to be fully-actuated or over-actuated, i.e., $l \geq 6$ and $\text{rank}(\mathbf{B}) = 6$. $\boldsymbol{\tau}_d$ denotes the external slowly-varying disturbance.

The water velocity in frame \mathcal{B} is assumed to be slowly-varying, i.e., $\dot{\mathbf{v}}_r \approx \dot{\mathbf{v}}$, and the dynamics of Eq. (6) can be rewritten as

$$\mathbf{M} \dot{\mathbf{v}} + \mathbf{C}_{RB}(\mathbf{v}) \mathbf{v} + \mathbf{C}_{AM}(\mathbf{v}_r) \mathbf{v}_r + \mathbf{D}(\mathbf{v}_r) \mathbf{v}_r + \mathbf{g}(\boldsymbol{\eta}_2) = \mathbf{B} \mathbf{T}(\boldsymbol{\delta}) + \boldsymbol{\tau}_d \quad (8)$$

with $\mathbf{M} = \mathbf{M}_{RB} + \mathbf{M}_{AM}$. It can also be expressed in a compact form as

$$\dot{\mathbf{v}} = \mathbf{F}(\boldsymbol{\eta}_2, \mathbf{v}, \boldsymbol{\delta}) \quad (9)$$

where

$$\mathbf{F}(\boldsymbol{\eta}_2, \mathbf{v}, \boldsymbol{\delta}) = \mathbf{M}^{-1}(\mathbf{B} \mathbf{T}(\boldsymbol{\delta}) + \boldsymbol{\tau}_d - \mathbf{C}_{RB}(\mathbf{v}) \mathbf{v} - \mathbf{C}_{AM}(\mathbf{v}_r) \mathbf{v}_r - \mathbf{D}(\mathbf{v}_r) \mathbf{v}_r - \mathbf{g}(\boldsymbol{\eta}_2)).$$

Considering modeling uncertainties, $\mathbf{F}(\boldsymbol{\eta}_2, \mathbf{v}, \boldsymbol{\delta})$ is the sum of an approximate model, $\bar{\mathbf{F}}(\boldsymbol{\eta}_2, \mathbf{v}, \boldsymbol{\delta})$, and the corresponding error, $\Delta \mathbf{F}(\boldsymbol{\eta}_2, \mathbf{v}, \boldsymbol{\delta})$, namely,

$$\dot{\mathbf{v}} = \bar{\mathbf{F}}(\boldsymbol{\eta}_2, \mathbf{v}, \boldsymbol{\delta}) + \Delta \mathbf{F}(\boldsymbol{\eta}_2, \mathbf{v}, \boldsymbol{\delta}) \quad (10)$$

with

$$\bar{\mathbf{F}}(\boldsymbol{\eta}_2, \mathbf{v}, \boldsymbol{\delta}) = \bar{\mathbf{M}}^{-1}(\bar{\mathbf{B}} \mathbf{T}(\boldsymbol{\delta}) + \bar{\boldsymbol{\tau}}_d - \bar{\mathbf{C}}_{RB}(\mathbf{v}) \mathbf{v} - \bar{\mathbf{C}}_{AM}(\mathbf{v}_r) \mathbf{v}_r - \bar{\mathbf{D}}(\mathbf{v}_r) \mathbf{v}_r - \bar{\mathbf{g}}(\boldsymbol{\eta}_2)) \quad (11)$$

and

$$\Delta \mathbf{F}(\boldsymbol{\eta}_2, \mathbf{v}, \boldsymbol{\delta}) = \mathbf{F}(\boldsymbol{\eta}_2, \mathbf{v}, \boldsymbol{\delta}) - \bar{\mathbf{F}}(\boldsymbol{\eta}_2, \mathbf{v}, \boldsymbol{\delta}) \quad (12)$$

where (\cdot) denotes the approximation of each parameter matrix or function in the dynamic model, e.g., $\bar{\mathbf{M}}$ is the estimated inertial matrix, and $\bar{\mathbf{v}}_r = \mathbf{v}$ and $\bar{\boldsymbol{\tau}}_d = \mathbf{0}$ when no current velocity or external disturbance information is available.

According to its universal approximation property (Haykin, 2009), an SHL perceptron neural network can approximate the nonlinear function $\Delta \mathbf{F}(\boldsymbol{\eta}_2, \mathbf{v}, \boldsymbol{\delta})$ with an arbitrarily small approximation error, $\epsilon(\boldsymbol{\eta}_2, \mathbf{v}, \boldsymbol{\delta})$, on a compact domain \mathcal{D} , as

$$\Delta \mathbf{F}(\boldsymbol{\eta}_2, \mathbf{v}, \boldsymbol{\delta}) = \mathbf{W}^T \boldsymbol{\sigma}(\mathbf{V}^T \mathbf{x}) + \epsilon(\boldsymbol{\eta}_2, \mathbf{v}, \boldsymbol{\delta}) \quad (13)$$

where \mathbf{W} and \mathbf{V} are the ideal inner-layer and out-layer weight matrices, respectively, defined as

$$\mathbf{V} \triangleq \begin{bmatrix} \theta_{v,1} & \cdots & \theta_{v,n_2} \\ \nu_{1,1} & \cdots & \nu_{1,n_2} \\ \vdots & \cdots & \vdots \\ \nu_{n_1,1} & \cdots & \nu_{n_1,n_2} \end{bmatrix} \in \mathbb{R}^{(n_1+1) \times n_2} \quad (14)$$

$$\mathbf{W} \triangleq \begin{bmatrix} \theta_{w,1} & \cdots & \theta_{w,n_3} \\ \omega_{1,1} & \cdots & \omega_{1,n_3} \\ \vdots & \cdots & \vdots \\ \omega_{n_2,1} & \cdots & \omega_{n_2,n_3} \end{bmatrix} \in \mathbb{R}^{(n_2+1) \times n_3} \quad (15)$$

with $n_1 = 9 + l$, n_2 , and $n_3 = 6$ being the node numbers of input, hidden, and output layer, respectively.

The input vector is defined as

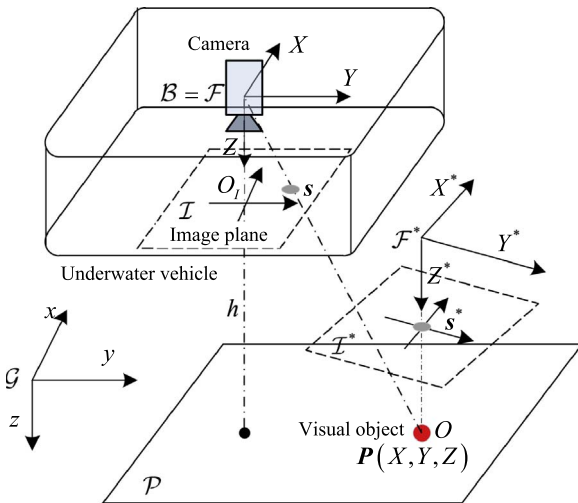


Fig. 1. Hybrid visual servoing of an underwater vehicle.

$$\bar{\mathbf{x}} = [b_v \quad \mathbf{x}_{in}^T]^T \in \mathbb{R}^{n_1+1} \quad (16)$$

with b_v being the input bias, $\mathbf{x}_{in} = [\boldsymbol{\eta}_2^T, \mathbf{v}^T, \boldsymbol{\delta}^T]^T \in \mathbb{R}^{n_1}$ is the neural network input.

The constant ideal weight matrices, \mathbf{W} and \mathbf{V} , are defined on a compact set $\mathcal{D} \subset \mathbb{R}^{n_1}$ of the input, and the corresponding upper bound of the approximation error is given as

$$\varepsilon^* \triangleq \sup_{\bar{\mathbf{x}} \in \mathcal{D}} \|\Delta \mathbf{F}(\boldsymbol{\eta}_2, \mathbf{v}, \boldsymbol{\delta}) - \mathbf{W}^T \boldsymbol{\sigma}(\mathbf{V}^T \bar{\mathbf{x}})\| \quad (17)$$

Hence, the approximation error, ε , is bounded by $\|\varepsilon\| \leq \varepsilon^*$ over \mathcal{D} . The general weight matrix defined by

$$\Xi \triangleq \begin{bmatrix} \mathbf{V} & \mathbf{0} \\ \mathbf{0} & \mathbf{W} \end{bmatrix} \quad (18)$$

is assumed to be bounded by a known positive value Ξ_M , i.e., $\|\Xi\|_F \leq \Xi_M$.

The sigmoid vector is defined as

$$\boldsymbol{\sigma}(\mathbf{y}) = \begin{bmatrix} b_w & \sigma(y_1) & \sigma(y_2) & \cdots & \sigma(y_{n_2}) \end{bmatrix}^T \quad (19)$$

with b_w being the output bias. The sigmoid activation function is defined as

$$\sigma(y_i) = \frac{1}{1 + e^{-ay_i}}, \quad i = 1, \dots, n_2 \quad (20)$$

where a is the activation potential and may have a distinct value for each neuron.

Note that the external disturbance in the dynamic model (9), $\boldsymbol{\tau}_d$, is assumed to be slowly-varying and is approximated by an SHL neural network as a constant dynamic parameter. The possible high-frequency disturbance and unmodeled dynamics that cannot be approximated by the neural network, is assumed to be bounded and included in the neural network approximation error, $\varepsilon(\boldsymbol{\eta}_2, \mathbf{v}, \boldsymbol{\delta})$.

2.2. Hybrid visual servoing model

The proposed HVS system for an underwater vehicle equipped with a downward-looking camera is depicted in Fig. 1. In this figure, \mathcal{F} and \mathcal{F}^* denote the local coordinate frames attached to the camera at the current pose, $\boldsymbol{\eta}$, and the target pose, $\boldsymbol{\eta}^*$, respectively; I and I^* are the current and target image planes. To simplify the calculations, the camera-fixed frame \mathcal{F} is assumed to coincide with the body-fixed frame \mathcal{B} , which means the camera's velocity expressed in \mathcal{F} equals the vehicle velocity expressed in \mathcal{B} . Without any loss of generality, the camera frame can be translated to any other location on the vehicle through an invertible coordinate transformation.

A point-like visual object beneath the vehicle, O , is used to indicate the vehicle's horizontal position information, and its global position is $\mathbf{O} = [x_o, y_o, z_o]^T$. The 3-D coordinates of O in the frames \mathcal{F} and \mathcal{F}^* are denoted by $\mathbf{P} = [X, Y, Z]^T$ and $\mathbf{P}^* = [X^*, Y^*, Z^*]^T$, which are calculated as $\mathbf{P} = \mathbf{R}_g^b(\boldsymbol{\eta}_2)(\mathbf{O} - \boldsymbol{\eta}_1)$ and $\mathbf{P}^* = \mathbf{R}_g^b(\boldsymbol{\eta}_2^*)(\mathbf{O} - \boldsymbol{\eta}_1^*)$, respectively. The time derivative of \mathbf{P} with respect to the camera frame is

$$\dot{\mathbf{P}} = -\mathbf{v}_1 - \mathbf{v}_2 \times \mathbf{P} \quad (21)$$

According to the perspective projection of a pin-hole camera (Chaumette and Hutchinson, 2006, 2007), the 2-D coordinates of the visual object projected in the current and target image frames expressed in pixel units, \mathbf{s} and \mathbf{s}^* , are given by

$$\begin{aligned} \mathbf{s} &\triangleq \begin{bmatrix} m \\ n \end{bmatrix} = \frac{\mathbf{A}_c}{Z} \begin{bmatrix} X \\ Y \end{bmatrix} = \begin{bmatrix} \mu \\ \gamma \end{bmatrix} - \begin{bmatrix} c_\mu \\ c_\gamma \end{bmatrix}, \\ \mathbf{s}^* &\triangleq \begin{bmatrix} m^* \\ n^* \end{bmatrix} = \frac{\mathbf{A}_c}{Z^*} \begin{bmatrix} X^* \\ Y^* \end{bmatrix} = \begin{bmatrix} \mu^* \\ \gamma^* \end{bmatrix} - \begin{bmatrix} c_\mu \\ c_\gamma \end{bmatrix} \end{aligned} \quad (22)$$

where $\mathbf{A}_c = \text{diag}\{\rho_m, \rho_n\}$ is the constant camera calibration matrix with

$\rho_m = \alpha_1 f$ and $\rho_n = \alpha_2 f$, $\alpha_1, \alpha_2 > 0$ are scaling factors, and $f > 0$ is the camera focal length. $[\mu, \gamma]^T$ and $[\mu^*, \gamma^*]^T$ denotes the current and desired pixel measurements of the image point. $[c_\mu, c_\gamma]^T$ is the principal point of the camera, including the possible constant image offset due to camera misalignment.

Differentiating Eq. (22) along Eq. (21) yields the following visual system model.

$$\dot{\mathbf{s}} = \mathbf{L}(\mathbf{s}, Z)\mathbf{v} \quad (23)$$

where $\mathbf{L}(\mathbf{s}, Z)$ is the image Jacobian matrix, also called the interaction matrix, containing the uncertain camera parameters, given by

$$\mathbf{L}(\mathbf{s}, Z) = \begin{bmatrix} -\frac{\rho_m}{Z} & 0 & \frac{m}{Z} & \frac{mn}{\rho_n} & -\frac{\rho_m^2 + m^2}{\rho_m} & \frac{\rho_m n}{\rho_n} \\ 0 & -\frac{\rho_n}{Z} & \frac{n}{Z} & \frac{\rho_n^2 + n^2}{\rho_n} & -\frac{mn}{\rho_m} & -\frac{\rho_n m}{\rho_m} \end{bmatrix}$$

The 2-D image data from a standard monocular visual system lacks any image depth information. To mitigate this issue, the image depth can be measured by a laser ranger or estimated by Kalman filtering (Gao et al., 2016b). In this paper, it is assumed that the underwater vehicle moves above the visual target, and the horizontal movement, the pitch and roll angles are kept small during operations. Thus, the image depth, Z , can be approximated by the vehicle's height above the seafloor, i.e., $Z \approx h$.

Integrating the visual and motion information into the global HVS pose, we have

$$\boldsymbol{\xi} \triangleq [m, n, h, \varphi, \theta, \psi]^T \in \mathbb{R}^6 \quad (24)$$

and the constant target pose is given by

$$\boldsymbol{\xi}^* \triangleq [m^*, n^*, h^*, \varphi^*, \theta^*, \psi^*]^T \in \mathbb{R}^6 \quad (25)$$

where h^*, φ^*, θ^* , and ψ^* are the desired height, roll, pitch, and yaw obtained at the target pose, respectively.

Using Eqs. (23), (5), and (1), the HVS kinematic equations can be written in a compact form as

$$\dot{\boldsymbol{\xi}} = \mathbf{J}_\xi(\boldsymbol{\xi})\mathbf{v} \quad (26)$$

where $\mathbf{J}_\xi(\boldsymbol{\xi})$ is the Jacobian matrix relating the body-fixed velocity to the rate of global HVS pose, defined by

$$\mathbf{J}_\xi(\boldsymbol{\xi}) = \begin{bmatrix} \mathbf{L}(\mathbf{s}, h) \\ -\mathbf{R}_3(\boldsymbol{\eta}_2) & \mathbf{0}_{1 \times 3} \\ \mathbf{0}_{3 \times 3} & \mathbf{T}_\theta(\boldsymbol{\eta}_2) \end{bmatrix} \in \mathbb{R}^{6 \times 6} \quad (27)$$

Note that the Jacobian matrix, $\mathbf{J}_\xi(\boldsymbol{\xi})$, is invertible if $\theta < \frac{\pi}{2}$ and $h > 0$.

The HVS control objective is to synthesize an adaptive feedback control law, based on the approximate dynamics, $\dot{\mathbf{v}} = \mathbf{F}(\boldsymbol{\eta}_2, \mathbf{v}, \boldsymbol{\delta})$, and the state feedback of $\boldsymbol{\xi}$, to drive the underwater vehicle to a constant target pose, i.e., $\boldsymbol{\xi}(t) \rightarrow \boldsymbol{\xi}^*$, and ensures the stability of tracking errors in the presence of system uncertainties.

3. Hybrid visual servo control development

3.1. Control system architecture

The block diagram of the overall proposed DI-SMANN is shown in Fig. 2. Within a DI-based MRAC architecture, described by Lewis (1999) and Johnson and Kannan (2005), a sliding model controller combined with a neural network compensator is employed to construct a pseudo control signal, ν , necessary to track a smooth reference trajectory, $\boldsymbol{\xi}_r(t)$, which is generated by the target pose, $\boldsymbol{\xi}^*$, through a reference model. A dynamic inversion module converts the pseudo control into actual thruster control signals by using the approximate dynamic model of underwater vehicles.

The second-order linear reference model is given by

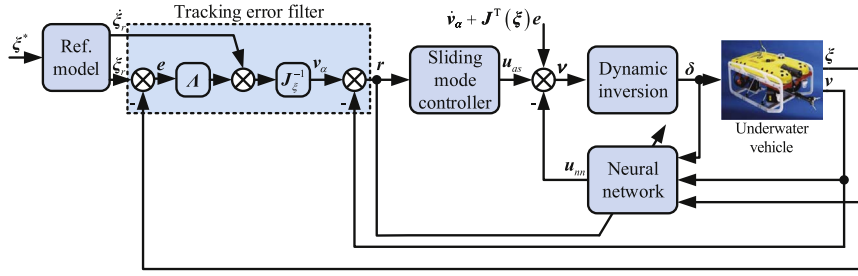


Fig. 2. Architecture of the proposed DI-SMANN for hybrid visual servoing of an underwater vehicle.

$$\ddot{\xi}_r = \mathbf{A}_p(\xi^* - \xi_r) - \mathbf{A}_d \dot{\xi}_r \quad (28)$$

where $\mathbf{A}_p = \text{diag}\{\omega_{r1}^2, \dots, \omega_{r6}^2\}$, $\mathbf{A}_d = \text{diag}\{2\zeta_{r1}\omega_{r1}, \dots, 2\zeta_{r6}\omega_{r6}\}$ are positive definite matrices, ω_{ri} , ζ_{ri} , $\forall i = 1, \dots, 6$ are the natural frequency and damping ratio of the reference model. The reference trajectory is initialized by the vehicle's initial states, i.e., $\xi_r(0) = \xi(0)$ and $\dot{\xi}_r(0) = \dot{\xi}(0)$.

The HVS trajectory tracking error is

$$\mathbf{e} \triangleq \xi_r - \xi = [e_m \ e_n \ e_h \ e_\varphi \ e_\theta \ e_\psi]^T \quad (29)$$

and a first-order filtered tracking error is defined as

$$\mathbf{r} \triangleq \mathbf{J}_\xi^{-1}(\xi)(\dot{\xi}_r - \mathbf{J}_\xi(\xi)\mathbf{v} + \Lambda\mathbf{e}) = \mathbf{v}_\alpha - \mathbf{v} \quad (30)$$

where Λ is a constant positive definite gain matrix and $\mathbf{v}_\alpha = \mathbf{J}_\xi^{-1}(\xi)(\dot{\xi}_r + \Lambda\mathbf{e})$ is the reference velocity. The dynamics of the filtered tracking error is calculated as

$$\dot{\mathbf{r}} = \dot{\mathbf{v}}_\alpha - \dot{\mathbf{v}} = \dot{\mathbf{v}}_\alpha - \bar{\mathbf{F}}(\eta_2, \mathbf{v}, \delta) - \Delta\mathbf{F}(\eta_2, \mathbf{v}, \delta) \quad (31)$$

Note that the derivative of the visual servoing error, $\dot{\mathbf{e}}$, can be formulated using the filtered error, \mathbf{r} , as

$$\dot{\mathbf{e}} = \dot{\xi}_r - \mathbf{J}_\xi(\xi)\mathbf{v} = \dot{\xi}_r - \mathbf{J}_\xi(\xi)(\mathbf{J}_\xi^{-1}(\xi)(\dot{\xi}_r + \Lambda\mathbf{e}) - \mathbf{r}) = -\Lambda\mathbf{e} + \mathbf{J}_\xi(\xi)\mathbf{r} \quad (32)$$

3.2. DI-SMANN design

As depicted in Fig. 2, the following desired global acceleration, namely the pseudo control, is designed to drive the system to the sliding surface defined by $\mathbf{r} = \mathbf{0}$, based on the approximate dynamic model.

$$\nu = \bar{\mathbf{F}}(\eta_2, \mathbf{v}, \delta) = \dot{\mathbf{v}}_\alpha + \mathbf{u}_{as} - \mathbf{u}_{nn}(\eta_2, \mathbf{v}, \delta) + \mathbf{J}_\xi^T(\xi)\mathbf{e} \quad (33)$$

where \mathbf{u}_{as} is the adaptive sliding model controller, defined by

$$\mathbf{u}_{as} = \mathbf{K}_s \mathbf{r} + \hat{\rho} \text{sgn}(\mathbf{r}) \quad (34)$$

with the diagonal positive definite matrices $\mathbf{K}_s = \text{diag}\{K_{s1}, \dots, K_{s6}\}$ and the adaptive switching gain $\hat{\rho}$. The signum function $\text{sgn}(\mathbf{r})$ is defined by

$$\text{sgn}(\mathbf{r}) \triangleq [\text{sgn}(r_1) \ \dots \ \text{sgn}(r_6)]^T \quad (35)$$

where r_1, \dots, r_6 are the elements of vector \mathbf{r} , $\text{sgn}(\cdot)$ is the scalar signum function. Considering the neural approximation of $\Delta\mathbf{F}$ in (13), the following neural network controller is designed to compensate for dynamic uncertainties.

$$\mathbf{u}_{nn} = \hat{\mathbf{W}}^T \boldsymbol{\sigma}(\hat{\mathbf{V}}^T \bar{\mathbf{x}}) - \mathbf{u}_{ar} \quad (36)$$

where $\hat{\mathbf{W}}$ and $\hat{\mathbf{V}}$ are the estimation matrices of \mathbf{W} and \mathbf{V} , $\hat{\Xi} = \text{diag}\{\hat{\mathbf{V}}, \hat{\mathbf{W}}\}$, and the corresponding estimation errors are $\bar{\mathbf{W}} = \mathbf{W} - \hat{\mathbf{W}}$, $\bar{\mathbf{V}} = \mathbf{V} - \hat{\mathbf{V}}$, $\bar{\Xi} = \Xi - \hat{\Xi}$. \mathbf{u}_{ar} is the robustifying signal designed as

$$\mathbf{u}_{ar} = \hat{K}_{r1} \|\hat{\Xi}\|_F \mathbf{r} + \hat{K}_{r2} \mathbf{r} \quad (37)$$

with two adaptive control gains of \hat{K}_{r1} and \hat{K}_{r2} .

The actual thruster control vector is calculated by the pseudo

control using an approximate dynamic inversion with respect to δ as

$$\delta = \bar{\mathbf{F}}^{-1}(\eta_2, \mathbf{v}, \nu) = \bar{\mathbf{T}}^{-1}(\bar{\mathbf{B}}^+(\bar{\mathbf{M}}\nu + \bar{\mathbf{C}}_{RB}(\mathbf{v})\mathbf{v} + \bar{\mathbf{C}}_{AM}(\mathbf{v}_r)\mathbf{v}_r + \bar{\mathbf{D}}(\mathbf{v}_r)\mathbf{v}_r + \bar{\mathbf{g}}(\eta_2) - \bar{\tau}_d)) \quad (38)$$

where $\bar{\mathbf{B}}^+ = \bar{\mathbf{B}}^T(\bar{\mathbf{B}}\bar{\mathbf{B}}^T)^{-1}$ is the pseudo inverse of $\bar{\mathbf{B}}$, which exists because $\bar{\mathbf{B}}$ is of full row rank for a fully-actuated underwater vehicle, i.e., $l > 6$. $\bar{\mathbf{T}}^{-1}: \mathbb{R}^l \rightarrow \mathbb{R}^l$ is the inverse function of $\bar{\mathbf{T}}$.

We have the following theorem about the stability of visual servoing errors and neural network weight matrices.

Theorem 1. Consider the HVS system of Eqs. (26) and (10) with the tracking errors in Eqs. (29) and (30), under the DI-SMANN controller given by Eqs. (33), (34) and (36)–(38). If the neural network weights, $\hat{\mathbf{W}}$ and $\hat{\mathbf{V}}$, are trained online by the following adaptive laws with e-modification terms (Johnson and Kannan, 2005; Lewis, 1999).

$$\begin{aligned} \dot{\hat{\mathbf{W}}} &= -\Pi_w((\boldsymbol{\sigma}(\hat{\mathbf{V}}^T \bar{\mathbf{x}}) - \boldsymbol{\sigma}'(\hat{\mathbf{V}}^T \bar{\mathbf{x}})\hat{\mathbf{V}}^T \bar{\mathbf{x}})^T \mathbf{r} + \kappa \|\mathbf{r}\| \hat{\mathbf{W}}) \\ \dot{\hat{\mathbf{V}}} &= -\Pi_v(\bar{\mathbf{x}} \mathbf{r}^T \hat{\mathbf{W}}^T \boldsymbol{\sigma}'(\hat{\mathbf{V}}^T \bar{\mathbf{x}}) + \kappa \|\mathbf{r}\| \hat{\mathbf{V}}) \end{aligned} \quad (39)$$

with $\Pi_w > 0$, $\Pi_v > 0$, and $\kappa > 0$ being the positive adaptation design parameters, $\boldsymbol{\sigma}'(\mathbf{z})$ denoting the derivative matrix of the sigmoid vector, the adaptive control gains are updated by

$$\dot{\hat{\rho}} = \alpha_1 \|\mathbf{r}\|, \quad \dot{\hat{K}}_{r1} = \alpha_2 \|\hat{\Xi}\|_F \|\mathbf{r}\|^2, \quad \dot{\hat{K}}_{r2} = \alpha_3 \|\mathbf{r}\|^2 \quad (40)$$

with α_1 , α_2 , and α_3 being positive adaptation factors, then the HVS tracking errors, \mathbf{e} and \mathbf{r} , are asymptotically stable, and the neural network weights, $(\hat{\mathbf{W}}, \hat{\mathbf{V}})$, are ultimately uniformly bounded on a compact set $\bar{\mathbf{x}} \in \mathcal{D}$.

Proof

Substituting the pseudo control Eqs. (33), (13), (36), and (37) into Eq. (31) yields

$$\begin{aligned} \dot{\mathbf{r}} &= -\mathbf{K}_s \mathbf{r} - \hat{\rho} \text{sgn}(\mathbf{r}) - \mathbf{J}_\xi^T(\xi)\mathbf{e} + \hat{\mathbf{W}}^T \boldsymbol{\sigma}(\hat{\mathbf{V}}^T \bar{\mathbf{x}}) - \hat{K}_{r1} \|\hat{\Xi}\|_F \mathbf{r} - \hat{K}_{r2} \mathbf{r} \\ &\quad - \bar{\mathbf{W}}^T \boldsymbol{\sigma}(\bar{\mathbf{V}}^T \bar{\mathbf{x}}) - \boldsymbol{\varepsilon}(\eta_2, \mathbf{v}, \delta) \end{aligned} \quad (41)$$

Let the Lyapunov function candidate be

$$V_1 = \frac{1}{2} \mathbf{e}^T \mathbf{e} + \frac{1}{2} \mathbf{r}^T \mathbf{r} + \frac{1}{2} \text{tr}\{\bar{\mathbf{W}}^T \Pi_w^{-1} \bar{\mathbf{W}}\} + \frac{1}{2} \text{tr}\{\bar{\mathbf{V}}^T \Pi_v^{-1} \bar{\mathbf{V}}\} \quad (42)$$

Differentiating Eq. (42) along Eqs. (32) and (41), we have

$$\begin{aligned} \dot{V}_1 &= -\mathbf{e}^T \Lambda \mathbf{e} - \mathbf{r}^T \mathbf{K}_s \mathbf{r} - \hat{\rho} \mathbf{r}^T \text{sgn}(\mathbf{r}) - \mathbf{r}^T (\bar{\mathbf{W}}^T \boldsymbol{\sigma}(\bar{\mathbf{V}}^T \bar{\mathbf{x}}) - \hat{\mathbf{W}}^T \boldsymbol{\sigma}(\hat{\mathbf{V}}^T \bar{\mathbf{x}}) + \boldsymbol{\varepsilon} + \mathbf{u}_{ar}) \\ &\quad - \text{tr}\{\bar{\mathbf{W}}^T \Pi_w^{-1} \dot{\bar{\mathbf{W}}}\} - \text{tr}\{\bar{\mathbf{V}}^T \Pi_v^{-1} \dot{\bar{\mathbf{V}}}\} = -\mathbf{e}^T \Lambda \mathbf{e} - \mathbf{r}^T \mathbf{K}_s \mathbf{r} - \hat{\rho} \mathbf{r}^T \text{sgn}(\mathbf{r}) \\ &\quad - \text{tr}\{\bar{\mathbf{W}}^T \Pi_w^{-1} \dot{\bar{\mathbf{W}}}\} - \text{tr}\{\bar{\mathbf{V}}^T \Pi_v^{-1} \dot{\bar{\mathbf{V}}}\} - \mathbf{r}^T (\bar{\mathbf{W}}^T (\boldsymbol{\sigma}(\bar{\mathbf{V}}^T \bar{\mathbf{x}}) - \boldsymbol{\sigma}'(\hat{\mathbf{V}}^T \bar{\mathbf{x}})\hat{\mathbf{V}}^T \bar{\mathbf{x}}) \\ &\quad + \hat{\mathbf{W}}^T \boldsymbol{\sigma}'(\hat{\mathbf{V}}^T \bar{\mathbf{x}})\bar{\mathbf{V}}^T \bar{\mathbf{x}} + \mathbf{w} + \mathbf{u}_{ar}) \end{aligned} \quad (43)$$

where $\mathbf{w} = \bar{\mathbf{W}}^T \boldsymbol{\sigma}'(\hat{\mathbf{V}}^T \bar{\mathbf{x}})\bar{\mathbf{V}}^T \bar{\mathbf{x}} + \bar{\mathbf{W}}^T \boldsymbol{\sigma}(\bar{\mathbf{V}}^T \bar{\mathbf{x}}) - \hat{\mathbf{W}}^T \boldsymbol{\sigma}(\hat{\mathbf{V}}^T \bar{\mathbf{x}}) + \boldsymbol{\varepsilon}$ is the disturbance term (Lewis, 1999), and is bounded by positive constants c_0 , c_1 , and c_2 as

$$\|\mathbf{w}\| \leq c_0 + c_1 \|\bar{\Xi}\|_F + c_2 \|\bar{\Xi}\|_F \|\mathbf{r}\| \quad (44)$$

Substituting Eq. (39) into Eq. (43) results in

$$\dot{V}_1 = -\mathbf{e}^T \mathbf{A} \mathbf{e} - \mathbf{r}^T \mathbf{K}_s \mathbf{r} - \hat{\rho} \mathbf{r}^T \text{sgn}(\mathbf{r}) - \mathbf{r}^T (\mathbf{w} + \mathbf{u}_p) + \kappa \|\mathbf{r}\| \text{tr}(\tilde{\Xi}^T \hat{\Xi}) \quad (45)$$

Using the following inequalities

$$\text{tr}(\tilde{\Xi}^T \hat{\Xi}) = \text{tr}(\tilde{\Xi}^T (\Xi - \tilde{\Xi})) \leq \|\tilde{\Xi}\|_F \Xi_M - \|\tilde{\Xi}\|_F^2 \quad (46)$$

$$\|\tilde{\Xi}\|_F \leq (\|\hat{\Xi}\|_F + \Xi_M) \quad (47)$$

$$\mathbf{r}^T \text{sgn}(\mathbf{r}) \geq \|\mathbf{r}\| \quad (48)$$

we have

$$\begin{aligned} \dot{V}_1 &\leq -\mathbf{e}^T \mathbf{A} \mathbf{e} - \mathbf{r}^T \mathbf{K}_s \mathbf{r} - \hat{\rho} \mathbf{r}^T \text{sgn}(\mathbf{r}) + \|\mathbf{r}\| (c_0 + c_1 \|\tilde{\Xi}\|_F + c_2 (\|\hat{\Xi}\|_F + \Xi_M) \|\mathbf{r}\|) \\ &\quad - \hat{K}_{r1} \|\hat{\Xi}\|_F \|\mathbf{r}\|^2 - \hat{K}_{r2} \|\mathbf{r}\|^2 + \kappa \|\mathbf{r}\| (\|\tilde{\Xi}\|_F \Xi_M - \|\tilde{\Xi}\|_F^2) \\ &\leq -\mathbf{e}^T \mathbf{A} \mathbf{e} - \mathbf{r}^T \mathbf{K}_s \mathbf{r} - \|\mathbf{r}\| \left(\hat{\rho} - c_0 - (c_1 + \kappa \Xi_M) \|\tilde{\Xi}\|_F + \kappa \|\tilde{\Xi}\|_F^2 \right) \\ &\quad + (c_2 - \hat{K}_{r1}) \|\hat{\Xi}\|_F \|\mathbf{r}\|^2 + (c_2 \Xi_M - \hat{K}_{r2}) \|\mathbf{r}\|^2 \leq -\mathbf{e}^T \mathbf{A} \mathbf{e} - \mathbf{r}^T \mathbf{K}_s \mathbf{r} \\ &\quad - \|\mathbf{r}\| \left(\kappa (\|\tilde{\Xi}\|_F - \rho_z)^2 + \varepsilon_s \right) + (\rho_0 + \varepsilon_s - \hat{\rho}) \|\mathbf{r}\| + (c_2 - \hat{K}_{r1}) \|\hat{\Xi}\|_F \|\mathbf{r}\|^2 \\ &\quad + (c_2 \Xi_M - \hat{K}_{r2}) \|\mathbf{r}\|^2 \end{aligned} \quad (49)$$

where ε_s is a positive constant, and

$$\rho_z = \frac{c_1 + \kappa \Xi_M}{2\kappa}, \rho_0 = c_0 + \frac{(c_1 + \kappa \Xi_M)^2}{4\kappa} \quad (50)$$

To validate the system stability with adaptive control gains, the following estimation errors are defined.

$$\begin{aligned} \tilde{\rho} &\triangleq \rho_0 + \varepsilon_s - \hat{\rho} \\ \tilde{K}_{r1} &\triangleq c_2 - \hat{K}_{r1} \\ \tilde{K}_{r2} &\triangleq c_2 \Xi_M - \hat{K}_{r2} \end{aligned} \quad (51)$$

The second positive definite Lyapunov function candidate is defined as

$$V_2 = V_1 + \frac{1}{2\alpha_1} \tilde{\rho}^2 + \frac{1}{2\alpha_2} \tilde{K}_{r1}^2 + \frac{1}{2\alpha_3} \tilde{K}_{r2}^2 \quad (52)$$

Differentiating Eq. (52) with respect to time gives

$$\begin{aligned} \dot{V}_2 &\leq -\mathbf{e}^T \mathbf{A} \mathbf{e} - \mathbf{r}^T \mathbf{K}_s \mathbf{r} - \|\mathbf{r}\| \left(\kappa (\|\tilde{\Xi}\|_F - \rho_z)^2 + \varepsilon_s \right) + \tilde{\rho} (\|\mathbf{r}\| - \alpha_1^{-1} \dot{\rho}) \\ &\quad + \tilde{K}_{r1} (\|\hat{\Xi}\|_F \|\mathbf{r}\|^2 - \alpha_2^{-1} \dot{K}_{r1}) + \tilde{K}_{r2} (\|\mathbf{r}\|^2 - \alpha_3^{-1} \dot{K}_{r2}) \end{aligned} \quad (53)$$

Substituting the adaptation laws of control gains in Eq. (40) into Eq. (53) yields

$$\dot{V}_2 \leq -\mathbf{e}^T \mathbf{A} \mathbf{e} - \mathbf{r}^T \mathbf{K}_s \mathbf{r} - \|\mathbf{r}\| \left(\kappa (\|\tilde{\Xi}\|_F - \rho_z)^2 + \varepsilon_s \right) \quad (54)$$

Thus, \dot{V}_2 is negative definite. By using the Barbalat's lemma, V_2 is bounded, and $\lim_{t \rightarrow \infty} \dot{V}_2 = 0$. Consequently, the HVS tracking errors, \mathbf{e} and \mathbf{r} , are asymptotically stable, and the neural network weights ($\hat{\mathbf{W}}$, $\hat{\mathbf{V}}$) are uniformly ultimately bounded on the compact set $\mathfrak{R} \in \mathcal{D}$.

Remark 1. Due to the discontinuity of signum functions, chattering phenomenon may occur in the control inputs. To overcome this problem, a boundary layer technique is employed by replacing the signum function $\text{sgn}(\mathbf{r})$ in \mathbf{u}_{as} with a saturation function $\text{sat}(\mathbf{r})$ defined by

$$\begin{aligned} \text{sat}(\mathbf{r}) &\triangleq [\text{sat}(r_1) \ \dots \ \text{sat}(r_6)]^T \\ \text{sat}(r_i) &= \begin{cases} \text{sgn}(r_i), & \text{for } |r_i| > \gamma_0 \\ r_i/\gamma_0, & \text{for } |r_i| \leq \gamma_0 \end{cases}, \quad \forall i = 1, \dots, 6 \end{aligned} \quad (55)$$

where $\gamma_0 > 0$ is the thickness of the boundary layer.

Remark 2. According to the adaptation laws of Eq. (40), we have $\dot{\rho} \geq 0$, $\dot{K}_{r1} \geq 0$, and $\dot{K}_{r2} \geq 0$. Therefore, the control gains are guaranteed to be positive, if their initial values are assigned to satisfy $\hat{\rho}(0) \geq 0$, $\hat{K}_{r1}(0) \geq 0$, $\hat{K}_{r2}(0) \geq 0$. However, in theory, the estimated control gains can be initialized using any values without violating the system stability.

Remark 3. According to the properties of SMC, the system trajectory will reach the sliding surface of $\mathbf{r} = 0$ in a finite time and stay on it, which ensures the boundedness of the control gains. However, in practice, a small deviation from the sliding surface caused by disturbances and measurement noises will cause the increasing of $\hat{\rho}$, \hat{K}_{r1} , and \hat{K}_{r2} , which could make the closed-loop system unstable. To prevent this issue and ensure the boundedness of control gains, the adaptive laws are augmented with dead zones for error signals and modified by including damping terms as follows.

$$\begin{aligned} \dot{\rho} &= \begin{cases} \alpha_1 \|\mathbf{r}\| - \xi_1 \hat{\rho} & \text{for } \|\mathbf{r}\| > \gamma_1 \\ 0, & \text{for } \|\mathbf{r}\| \leq \gamma_1 \end{cases} \\ \dot{K}_{r1} &= \begin{cases} \alpha_2 \|\hat{\Xi}\|_F \|\mathbf{r}\|^2 - \xi_2 \hat{K}_{r1} & \text{for } \|\mathbf{r}\| > \gamma_2 \\ 0, & \text{for } \|\mathbf{r}\| \leq \gamma_2 \end{cases} \\ \dot{K}_{r2} &= \begin{cases} \alpha_3 \|\mathbf{r}\|^2 - \xi_3 \hat{K}_{r2} & \text{for } \|\mathbf{r}\| > \gamma_3 \\ 0, & \text{for } \|\mathbf{r}\| \leq \gamma_3 \end{cases} \end{aligned} \quad (56)$$

where γ_1 , γ_2 , and γ_3 are the small positive limits of dead zones, ξ_1 , ξ_2 , and ξ_3 are the positive damping coefficients.

Remark 4. The proposed DI-SMANN scheme could be applied for the trajectory tracking control of nonlinear robotic manipulators, which are modeled as follows (Wai and Muthusamy, 2013; Sun et al., 2011).

$$\mathbf{M}(\mathbf{q})\ddot{\mathbf{q}} + \mathbf{C}(\mathbf{q}, \dot{\mathbf{q}})\dot{\mathbf{q}} + \mathbf{G}(\mathbf{q}) + \mathbf{F}(\dot{\mathbf{q}}) = \boldsymbol{\tau} + \mathbf{T}_d \quad (57)$$

where \mathbf{q} , $\dot{\mathbf{q}}$, and $\ddot{\mathbf{q}}$ denote the joint position, velocity, and acceleration vectors, respectively. $\mathbf{M}(\mathbf{q})$ represents the inertia matrix. $\mathbf{C}(\mathbf{q}, \dot{\mathbf{q}})$ represents centripetal-Coriolis matrix. $\mathbf{G}(\mathbf{q})$ denotes the gravity effects. $\mathbf{F}(\dot{\mathbf{q}})$ represents the friction effects. \mathbf{T}_d is a vector of unknown additive bounded disturbances. $\boldsymbol{\tau}$ is the torque input vector. The reference trajectory is described by $\mathbf{q}_r(t)$ and its derivatives. The corresponding filtered tracking error is formulated as

$$\mathbf{r} \triangleq \ddot{\mathbf{q}}_r - \dot{\mathbf{q}} + \Lambda(\mathbf{q}_r - \mathbf{q}) \quad (58)$$

where Λ is also a constant positive definite gain matrix. The DI-SMANN trajectory tracking controller for the manipulator in (57) can be designed by using a similar method.

4. Simulation studies

In this section, the performance of this proposed HVS controller is verified by numerical simulations using the *Kambara* underwater vehicle developed at the Australian National University (Silpa-Anan, 2001). The parameters of *Kambara* are given below, in which the thrust mapping matrix is modified by adding a sway thruster to make the vehicle fully-actuated.

$$\mathbf{M}_{RB} = \text{diag}\{117, 117, 117, 10.7, 11.8, 13.4\},$$

$$\mathbf{M}_{AM} = \text{diag}\{58.4, 23.8, 23.8, 3.38, 1.18, 2.67\},$$

$$\mathbf{D}(\mathbf{v}) = \text{diag}\{120 + 90|u|, 90 + 90|v|, 150 + 120|w|, 15 + 10|p|, 15 + 12|q|, 18 + 15|r|\},$$

$$\mathbf{B} = \begin{bmatrix} 1 & 1 & 0 & 0 & 0 & 0 \\ 0 & 0 & 0 & 0 & 0 & 1 \\ 0 & 0 & -1 & -1 & -1 & 0 \\ 0 & 0 & -0.28 & 0.28 & 0 & 0.05 \\ -0.05 & -0.05 & -0.32 & -0.32 & 0.43 & 0 \\ 0.47 & -0.47 & 0 & 0 & 0 & 0 \end{bmatrix}$$

The weight of the vehicle is 117 kg, and the buoyant force is

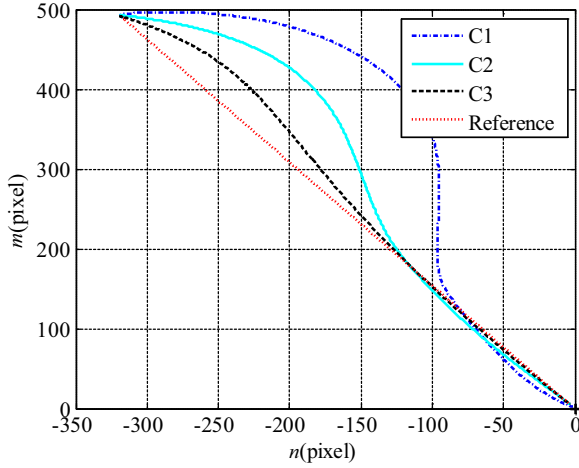


Fig. 3. Image trajectory of the feature.

1158 N. The center of the gravity is at the origin of the body frame and the center of buoyancy is located at $\mathbf{r}_B = [-0.017, 0, -0.115]^T$. The thrust function is $T_i(\delta_i) = 8\delta_i|\delta_i|$, $\forall i = 1, \dots, 6$ with δ_i and T_i being the control voltage and thrust force of the i th thruster. The control voltage is bounded by $|\delta_i| \leq 5V$ so that the maximum thrust force is 200 N. The approximate thrust function for the i th thruster is $\bar{T}_i(\delta_i) = 10\delta_i|\delta_i|$ in the DI-SMANN. A constant water velocity of $\mathbf{v}_c = [0.1, 0.1, 0]^T$ is considered. To test the adaptation performance of the neural network, the following approximate parameters are used in the simulations.

$$\bar{\mathbf{M}}_{RB} = \text{diag}\{110, 110, 110, 10, 10, 15\},$$

$$\bar{\mathbf{M}}_{AM} = \text{diag}\{60, 20, 20, 3, 1, 3\},$$

$$\bar{\mathbf{D}}(\mathbf{v}) = \text{diag}\{90 + 70|u|, 100 + 70|v|, 120 + 90|w|, 10 + 8|p|, 10 + 10|q|, 20 + 10|r|\}$$

$$\bar{\mathbf{B}} = \begin{bmatrix} 1 & 1 & 0 & 0 & 0 & 0 \\ 0 & 0 & 0 & 0 & 0 & 1 \\ 0 & 0 & -1 & -1 & -1 & 0 \\ 0 & 0 & -0.3 & 0.3 & 0 & 0 \\ 0 & 0 & -0.3 & -0.3 & 0.5 & 0 \\ 0.5 & -0.5 & 0 & 0 & 0 & 0 \end{bmatrix}$$

The actual camera calibration parameters are $\rho_m = \rho_n = 1000$ pixel,

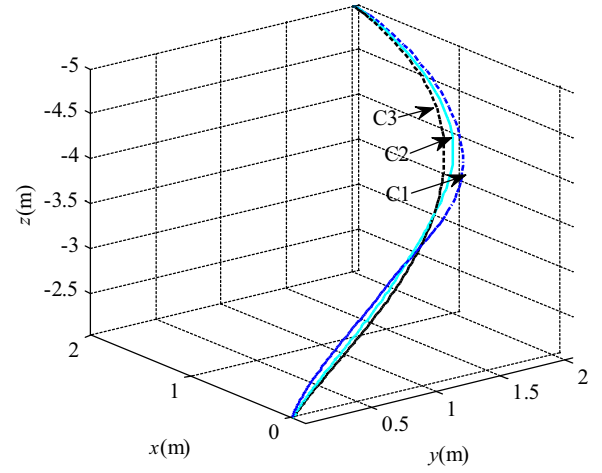


Fig. 4. 3-D trajectory of the underwater vehicle.

and the approximate values of $\bar{\rho}_m = \bar{\rho}_n = 800$ pixel are used in the HVS controller. Note that this modeling error would cause position control errors when PBVS is performed. In this simulation, a single visual feature is located on the seafloor and is chosen as the origin of the global frame, i.e., $\mathbf{O} = [0, 0, 0]^T$. The target HVS pose is $\xi^* = [0, 0, -2, 0, 0, 0]^T$. The initial global pose of the vehicle is $\eta(0) = [-2, -1, -5, \pi/36, -\pi/36, \pi/2]^T$.

The control and adaptation parameters of DI-SMANN are set as $\mathbf{A}_p = 0.16\mathbf{I}_6$, $\mathbf{A}_d = 1.2\mathbf{I}_6$, $n_2 = 20$, $\mathbf{\Pi}_w = 0.2\mathbf{I}_{n_2+1}$, $\mathbf{\Pi}_v = 2\mathbf{I}_{n_1+1}$, $\kappa = 1$, $\hat{\rho}(0) = \hat{\kappa}_{r1}(0) = \hat{\kappa}_{r2}(0) = 0$, $\alpha_1 = \alpha_2 = \alpha_3 = 0.1$, $\gamma_0 = 0.01$, $\gamma_1 = \gamma_2 = \gamma_3 = 0.001$.

The following control parameters of Λ and \mathbf{K}_s are used in comparative simulations to investigate the system performances of the proposed HVS controller,

$$\text{C1: } \Lambda = \text{diag}\{0.25, 0.25, 0.25, 0.5, 0.5, 0.5\}, \mathbf{K}_s = \text{diag}\{1, 1, 1, 2, 2, 2\};$$

$$\text{C2: } \Lambda = \text{diag}\{0.5, 0.5, 0.5, 1, 1, 1\}, \mathbf{K}_s = \text{diag}\{2, 2, 2, 4, 4, 4\};$$

$$\text{C3: } \Lambda = \text{diag}\{1, 1, 1, 2.5, 2.5, 2.5\}, \mathbf{K}_s = \text{diag}\{4, 4, 4, 10, 10, 10\}.$$

The simulation results are plotted in Figs. 3–9. It is observed in Fig. 3 that the visual feature in the image plane satisfactorily tracks the reference trajectory under the proposed HVS controller, and the visual tracking errors could be reduced by increasing the control gains of Λ

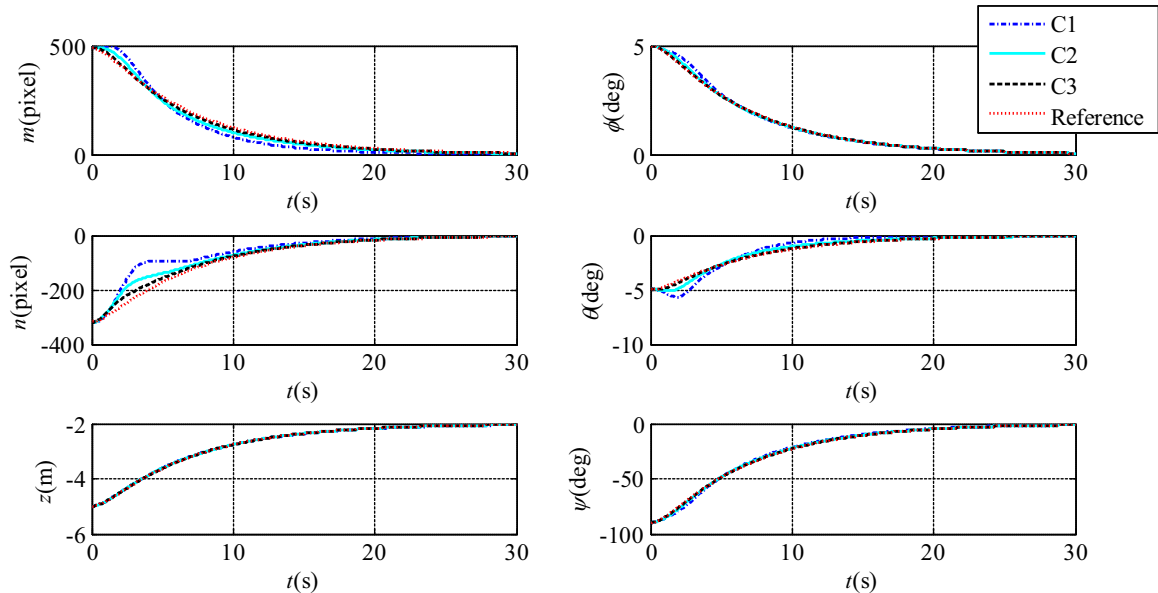


Fig. 5. Actual and reference global HVS poses.

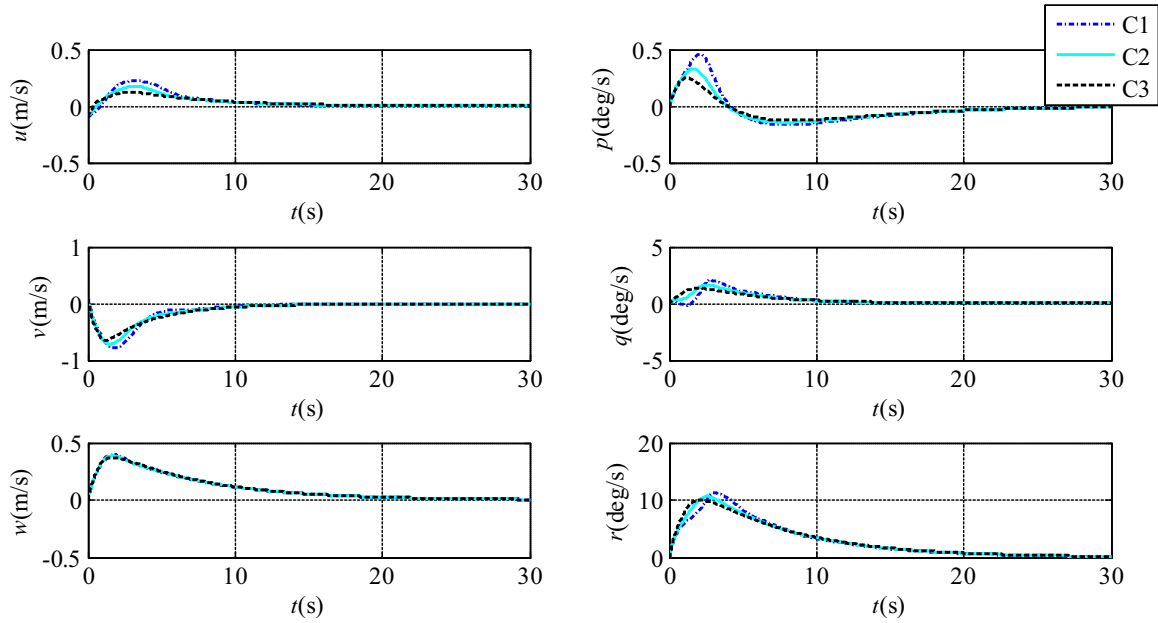


Fig. 6. Actual and reference velocities.

and \mathbf{K}_y . The 3-D position and Euler angles, as shown in Fig. 4 and Fig. 5, are all stabilized to the desired values despite camera calibration errors. As shown in Fig. 6, the linear and angular velocities converge to zero when the vehicle reaches the target pose. However, the behavior of the 3-D trajectory in Fig. 4 is less satisfactory with a circuitous curve, which is caused by the HVS controller trying to track the straight reference image trajectory while maneuvering in yaw. The velocities of the underwater vehicle are plotted in Fig. 6, which converge to zeroes when the vehicle reaches the desired pose.

The time integrals of the absolute tracking errors under the proposed controllers with different control gains are compared in Table 1. The data in Table 1 indicate that the tracking errors decrease with the increasing control gains, which means greater efforts during the control process.

The thruster control signals, as shown in Fig. 7, converge to non-zero values to overcome the steady restoring and hydrodynamic forces

generated by water currents. The adaptive gains grow from their initial values to some positive constants, which can ensure the asymptotical stability of the tracking errors, as shown in Fig. 8. In summary, the proposed adaptive HVS controller successfully drives the vehicle to the target pose in the presence of dynamic modeling uncertainties and camera calibration errors. The approximate errors of the neural network, $\mathbf{e}_{nn} = \mathbf{u}_{nn} - \Delta\mathbf{F}$, in the C3 DI-SMANN controller are plotted in Fig. 9, which shows that the approximate errors are bounded, and the neural network stops learning when the tracking errors converge to zeroes.

Finally, the simulated image depth, Z , and the height, h , of the underwater vehicle under the C3 controller are compared in Fig. 10 to validate the approximation, $Z \approx h$, which we made in the HVS controller design.

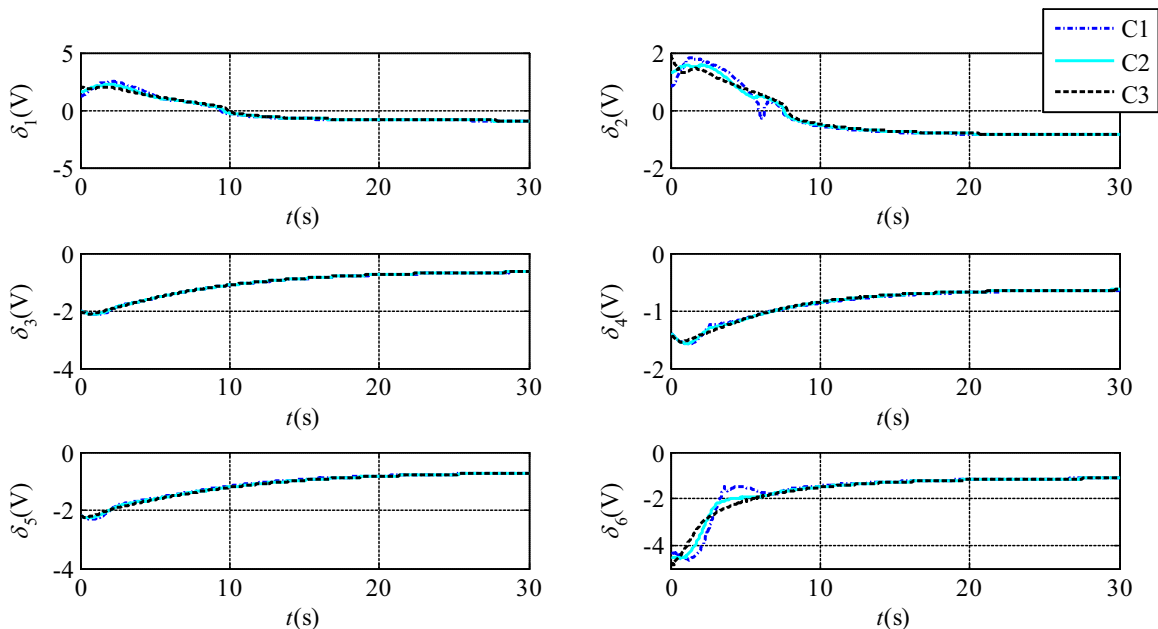


Fig. 7. Thruster control signals.

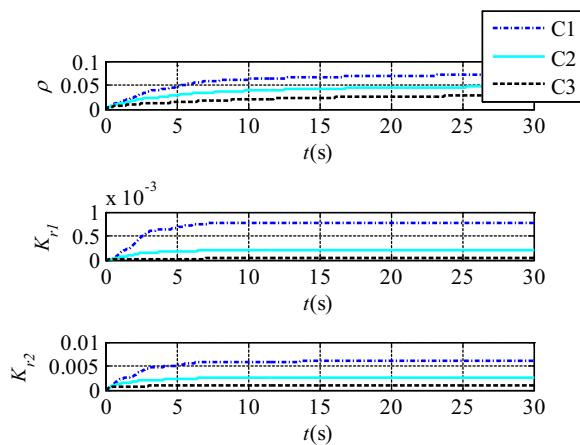


Fig. 8. Adaptive control gains.

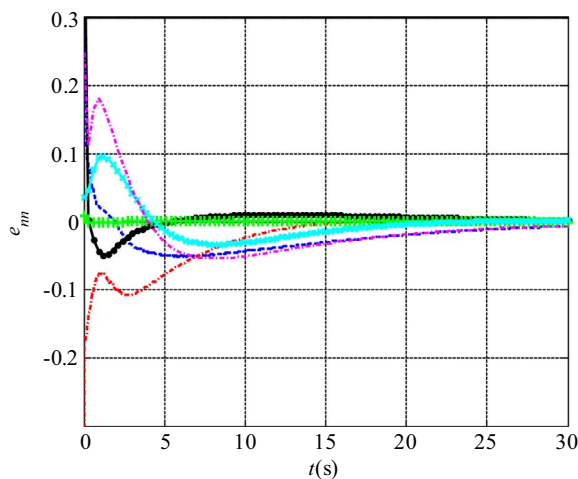


Fig. 9. Approximation errors of the neural network.

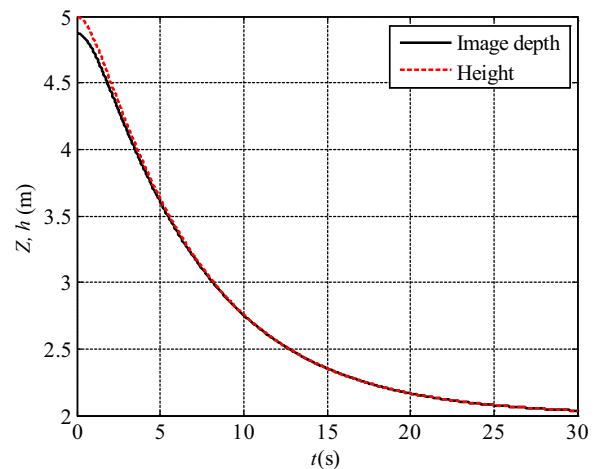


Fig. 10. Image depth of the visual object and height above the seafloor.

uncertainties and neural network weight matrices is required, which make it a competitive choice for underwater vehicles and other robotic systems.

Note that the thruster dynamics of underwater vehicles are omitted in this paper. However, as pointed out in Yoerger et al. (1990) and Whitcomb and Yoerger (1999), this could lead to limit cycles in the closed-loop positioning system, and degrade the control performance. One difficulty of the feedback compensation for thruster dynamics is due to thruster model uncertainties, including thrust and load torque coefficients, rotor moments of inertia, control torque constants, and the friction coefficients. We will work on a dual-loop NN-based adaptive positioning control system, where thruster dynamics and inherent nonlinearities are compensated by using neural networks in the inner-loop thruster velocity controller.

Table 1

Comparison of the tracking errors with different control gains.

Controller	$\int e_m dt$ (m)	$\int e_n dt$ (m)	$\int e_h dt$ (m)	$\int e_\phi dt$ (deg)	$\int e_\theta dt$ (deg)	$\int e_\psi dt$ (deg)
C1	748.9	647.5	0.2247	1.3885	9.6679	24.8930
C2	365.2	314.8	0.1181	0.5576	4.1544	9.6414
C3	145.1	153.0	0.0555	0.1179	1.0091	2.1912

5. Conclusion

In this paper, an HVS system for underwater vehicles with various motion sensors is developed. The proposed approach differs from conventional visual servoing methods in that the system errors are constructed from a combination of visual pixel information and measured pose variables (i.e., height and orientation angles), which makes the system more practical in underwater applications.

To solve the nonlinear HVS control problem, a DI-SMANN controller with adaptive control gains is designed with compensation for dynamic uncertainties. The visual servoing error is proven to be asymptotically stable by using the Lyapunov method. The main advantage of this proposed DI-SMANN over conventional NN-based controllers is that no *a priori* knowledge of the bounds on system

Acknowledgment

This work is supported in part by the National Natural Science Foundation of China under the Grants of 61633002 and 51279164, and in part by the Fundamental Research Funds for the Central Universities under the Grant of 3102017gx06001. The authors would like to thank the editor and reviewers for their constructive comments and suggestions that have improved the quality of the paper.

References

- Anderson, R.T., Chowdhary, G.V., Johnson, E.N., 2009. Comparison of RBF and SHL neural network based adaptive control. *J. Intell. Robot. Syst.* 54 (3), 183–199.
- Bechlioulis, C.P., Karras, G.C., Nagappa, S., Palomeras, N., Kyriakopoulos, K.J., Carreras, M., 2013. A robust visual servo control scheme with prescribed performance for an autonomous underwater vehicle. In: *Proceedings of the IEEE/RSJ International Conference on Intelligent Robots and Systems*. pp. 3879–3884.

- Caccia, M., 2007. ROV horizontal motion control: near-seafloor experimental results. *Control Eng. Pract.* 15 (6), 703–714.
- Chaumette, F., Hutchinson, S., 2006. Visual servo control. I. Basic approaches. *IEEE Robot. Autom. Mag.* 13 (4), 82–90.
- Chaumette, F., Hutchinson, S., 2007. Visual servo control. II. Advanced approaches. *IEEE Robot. Autom. Mag.* 14 (1), 109–118.
- Chu, Z., Zhu, D., Yang, S.X., 2016. Observer-based adaptive neural network trajectory tracking control for remotely operated vehicle. *IEEE Trans. Neural Netw. Learn. Syst.* <http://dx.doi.org/10.1109/TNNLS.2016.2544786>.
- Cui, R., Zhang, X., Cui, D., 2016. Adaptive sliding-mode attitude control for autonomous underwater vehicles with input nonlinearities. *Ocean Eng.* 123, 45–54.
- Du, J., Yang, Y., Wang, D., Guo, C., 2013. A robust adaptive neural networks controller for maritime dynamic positioning system. *Neurocomputing* 110, 128–136.
- Fischer, N., Hughes, D., Walters, P., Schwartz, E.M., Dixon, W.E., 2014. Nonlinear RISE-based control of an autonomous underwater vehicle. *IEEE Trans. Robot.* 30 (4), 845–852.
- Fossen, T.I., 2002. *Marine Control Systems: Guidance, Navigation and Control of Ships, Rigs and Underwater Vehicles*. Marine Cybernetics, Trondheim, Norway.
- Gao, J., Proctor, A., Shi, Y., Bradley, C., 2016a. Hierarchical model predictive image-based visual servoing of underwater vehicles with adaptive neural network dynamic control. *IEEE Trans. Cybern.* 46 (10), 2323–2334.
- Gao, J., Wu, P., Yang, B., Xia, F., 2016b. Adaptive neural network control for visual servoing of underwater vehicles with pose estimation. *J. Mar. Sci. Technol.* <http://dx.doi.org/10.1007/s00773-016-0426-6>.
- Gao, J., Li, T., Wu, P., Zhang, L., Yan, W., 2016c. A hybrid approach for visual servo control of underwater vehicles. In: *Proceedings of the MTS/IEEE Oceans Conference*. pp. 1–6.
- Haykin, S., 2009. *Neural Networks and Learning Machines* 3rd ed.. Pearson, Upper Saddle River, NJ, USA.
- Heshmati-alamdari, S., Eqtami, A., Karras, G.C., Dimarogonas, D.V., Kyriakopoulos, K. J., 2014. A self-triggered visual servoing model predictive control scheme for under-actuated underwater robotic vehicles. In: *Proceedings of the 2014 IEEE International Conference on Robotics and Automation*. pp. 3826–3831.
- Hua, M.D., Allibert, G., Krupinski, S., Hamel, T., 2014. Homography-based visual servoing for autonomous underwater vehicles. In: *Proceedings of the 19th IFAC World Congress*. pp. 5726–5733.
- Johnson, E.N., Kannan, S.K., 2005. Adaptive trajectory control for autonomous helicopters. *J. Guid. Control Dyn.* 28 (3), 524–538.
- Lewis, F.L., 1999. Nonlinear network structures for feedback control. *Asian J. Control* 1 (4), 205–228.
- Li, Y., Xu, Q., 2010. Adaptive sliding mode control with perturbation estimation and PID sliding surface for motion tracking of a piezo-driven micromanipulator. *IEEE Trans. Control Syst. Technol.* 18 (4), 798–810.
- Li, Y., Jiang, Y., Cao, J., Wang, B., Li, Y., 2015. AUV docking experiments based on vision positioning using two cameras. *Ocean Eng.* 110, 163–173.
- Lots, J.-F., Lane, D.M., Trucco, E., 2000. Application of 2 1/2 D visual servoing to underwater vehicle station-keeping. In: *Proceedings of the MTS/IEEE Oceans Conference*. pp. 1257–1264.
- Lots, J.-F., Lane, D.M., Trucco, E., Chaumette, F., 2001. A 2-D visual servoing for underwater vehicle station keeping. In: *Proceedings of the IEEE International Conference on Robotics and Automation*. pp. 2767–2772.
- Patre, P.M., MacKunis, W., Kaiser, K., Dixon, W.E., 2008. Asymptotic tracking for uncertain dynamic systems via a multilayer neural network feedforward and RISE feedback control structure. *IEEE Trans. Autom. Control* 53 (9), 2180–2185.
- Peng, Z., Wang, J., 2017. Output-feedback path-following control of autonomous underwater vehicles based on an extended state observer and projection neural networks. *IEEE Trans. Syst., Man, Cybern.: Syst.* <http://dx.doi.org/10.1109/TSMC.2017.2697447>.
- Proctor, A.A., 2014. *Semi-Autonomous Guidance and Control of a Saab SeaEye Falcon ROV* (Doctor's thesis). University of Victoria, Victoria, BC, Canada.
- Shen, Y., Shao, K., Ren, W., Liu, Y., 2016a. Diving control of autonomous underwater vehicle based on improved active disturbance rejection control approach. *Neurocomputing* 173, 1377–1385.
- Shen, C., Buckham, B., Shi, Y., 2016b. Modified C/GMRES algorithm for fast nonlinear model predictive tracking control of AUVs. *IEEE Trans. Cont. Syst. Technol.* <http://dx.doi.org/10.1109/TCST.2016.2628803>.
- Shen, C., Shi, Y., Buckham, B., 2017. Integrated path planning and tracking control of an AUV: A unified receding horizon optimization approach. *IEEE/ASME Trans. Mechatron.* 22 (3), 1163–1173.
- Shi, Y., Shen, C., Fang, H., Li, H., 2017. Advanced control in marine mechatronic systems: A survey. *IEEE/ASME Trans. Mechatron.* 22 (3), 1121–1131.
- Silpa-Anan, C., 2001. *Autonomous Underwater Robot: Vision and Control* (Master's thesis). Australian National University, Australia.
- Silpa-Anan, C., Brinsmead, T., Abdallah, S., Zelinsky, A., 2001. Preliminary experiments in visual servo control for autonomous underwater vehicle. In: *Proceedings of the IEEE/RSJ International Conference on Intelligent Robots and Systems*. pp. 1824–1829.
- Sørensen, A.J., 2011. A survey of dynamic positioning control systems. *Annu. Rev. Control* 35 (1), 123–136.
- Soylu, S., Proctor, A.A., Podhorodeski, R.P., Bradley, C., Buckham, B.J., 2016. Precise trajectory control for an inspection class ROV. *Ocean Eng.* 111, 508–523.
- Sun, T., Pei, H., Pan, Y., Zhou, H., Zhang, C., 2011. Neural network-based sliding mode adaptive control for robot manipulators. *Neurocomputing* 74 (14–15), 2377–2384.
- Valentinis, F., Donaire, A., Perez, T., 2015. Energy-based motion control of a slender hull unmanned underwater vehicle. *Ocean Eng.* 104, 604–616.
- Wai, R.-J., Muthusamy, R., 2013. Fuzzy-neural-network inherited sliding-mode control for robot manipulator including actuator dynamics. *IEEE Trans. Neural Netw. Learn. Syst.* 24 (2), 274–287.
- Whitcomb, L.L., Yoerger, D.R., 1999. Preliminary experiments in model-based thruster control for underwater vehicle positioning. *IEEE J. Ocean. Eng.* 24 (4), 495–506.
- Yoerger, D.R., Cooke, J.G., Slotine, J.-J.E., 1990. The influence of thruster dynamics on underwater vehicle behavior and their incorporation into control system design. *IEEE J. Ocean. Eng.* 15 (3), 167–178.
- Zhang, L., Qi, X., Pang, Y., 2009. Adaptive output feedback control based on DRFNN for AUV. *Ocean Eng.* 36, 716–722.
- Zhang, M., Chu, Z., 2012. Adaptive sliding mode control based on local recurrent neural networks for underwater robot. *Ocean Eng.* 45, 56–62.
- Zhu, D., Sun, B., 2013. The bio-inspired model based hybrid sliding-mode tracking control for unmanned underwater vehicles. *Eng. Appl. Artif. Intell.* 26, 2260–2269.
- Zool, H., Ismail, M.B., Mokhar, M., Putranti, V.W.E., Dunnigan, M.W., 2016. A robust dynamic region-based control scheme for an autonomous underwater vehicle. *Ocean Eng.* 111, 155–165.